Soft Matter

Designing Active Particles for Colloidal Microstructure Manipulation via Strain Field Alchemy

Journal:	*Soft Matter*
Manuscript ID	SM-ART-05-2019-000896.R2
Article Type:	Paper
Date Submitted by the Author:	25-Jun-2019
Complete List of Authors:	Vansaders, Bryan; University of Michigan College of Engineering, Materials Science and Engineering Glotzer, Sharon; University of Michigan, Chemical Engineering

Journal Name

ARTICLE TYPE

Cite this: DOI: 00.0000/xxxxxxxxxx

Designing Active Particles for Colloidal Microstructure Manipulation *via* Strain Field Alchemy†

Bryan VanSaders[a] and Sharon C. Glotzer*[abc]

Received Date
Accepted Date

DOI: 00.0000/xxxxxxxxxx

Defects in a crystal can exert forces on each other *via* strain field interactions. Here we explore the strain-field-mediated interaction between an anisotropic interstitial probe particle and dislocation microstructures in a colloidal crystal composed of particles interacting *via* steep repulsive isotropic potentials. We optimize the interaction between probe particle and dislocation with the anisotropic shape of the probe as a free parameter. Such alchemical optimization is typically carried out upon the explicitly defined interaction potential parameters; instead, we optimize the strain field of the probe and then map back to particle shape. We distinguish this tactic from other alchemical methods as 'strain alchemy'. We report several findings: 1) a robust mapping exists between strain field calculation methods (the method of eigenstrains) and strains produced by an anisotropic interstitial, 2) optimization of strain field interactions in the strain domain permits rapid evaluation of candidate shapes for interstitials, 3) interstitial mobility barriers can be estimated from the strain field, and 4) strongly interacting and highly mobile interstitial particles can be found that are capable of driving dislocation glide with applied force. Active particle-induced dislocation glide is examined for the cases of edge dislocation arrays and extrinsic dislocation loops. For edge dislocations, particle geometries of alternating large and small diameter segments were found to interact most strongly. For dislocation loops, interstitials with a single small radius segment surrounded by large radius segments are best.

1 Introduction

Rational design of colloidal crystals has focused primarily on crystal structure, with many excellent examples in the literature exploring the connection between particle interaction potentials (isotropic, anisotropic, DNA-based, hard shape, *etc.*) and equilibrium crystal structures[1–14]. Far sparser are studies exploring the connection between these design parameters and material properties. The optical response of colloidal crystals[15–18] has received the most attention, but mechanical and acoustical properties are also of interest[19–22]. Rarer still are studies concerning the design of kinetically trapped defect states in colloidal materials. Such states are generally known as defect 'microstructure' in the metallurgical research community, and include phenomena such as dislocation networks and grain boundary interfaces. In metals, defect microstructure plays a critically important role in determining mechanical properties such as ultimate tensile strength and creep[23]. Defect microstructure can also strongly influence other materials properties—such as conductivity—across orders of magnitude[24].

In photonic colloidal crystals, defects can create transmissive breaks in a photonic band-gap. These localized non-evanescent modes can be exploited to create device components such as wave guides and resonator cavities[25–27]. Connected regions of defects, such as those used in wave guides, can be thought of as a type of defect microstructure, with profound consequences for the optical band properties of the metamaterial. If the defects responsible for such properties could be reconfigured, then colloidal materials with tunable or dynamic properties are in principle possible.

Methods of microstructure control can be broadly grouped into two categories: microstructure formation during a phase transition, and microstructure formation without a phase transition. The first group encompasses many methods of control including Ostwald ripening[28], precipitation from solid solution[29], spinodal decomposition[30], and epitaxial growth[31]. Generally these methods employ a competition of mechanisms with different kinetics or enforced boundary conditions that modify the free-energy of a system to achieve the desired microstructure as the final solid phase is forming from the precursor phase (either fluid or a dif-

[a] *Department of Materials Science and Engineering, University of Michigan, Ann Arbor, Michigan 48109, United States*
[b] *Department of Chemical Engineering, University of Michigan, Ann Arbor, Michigan 48109, United States*
[c] *Biointerfaces Institute, University of Michigan, Ann Arbor, Michigan 48109, United States, E-mail: sglotzer@umich.edu*

† Electronic Supplementary Information (ESI) available: [details of any supplementary information available should be included here]. See DOI: 00.0000/00000000.

ferent solid). The second group of methods relies upon the application of non-thermal forces to drive microstructure evolution. Strain hardening in metals is a prototypical example of such a process[23], where forces are applied that drive microstructure evolution while the material is held at temperatures too low to permit escape from the metastable states formed. The use of high shear rates or high-energy bombardment with radiation has been explored to control microstructure in what are termed 'driven alloys'[32–34].

Despite the enormous wealth of materials science knowledge available (and numerous reports on colloidal defect behavior[35–41]), microstructure engineering in colloidal systems is only lightly explored. Van Blaaderen *et al.*[42] and more recently Dasgupta *et al.*[43] have explored the effect of surface templating on colloidal growth by sedimentation. By templating a surface with the periodicity of non-close-packed planes stacking faults can be suppressed as the crystal grows. The impact of large impurities on 2D colloidal crystal growth has also been explored[37,44]. Large impurity particles locally stabilize fluid-like configurations, and as a result are often incorporated into (and pin the motion of) grain boundaries during crystallization. These methods, where a defect microstructure is assembled from a fluid state, would fall under the first category of microstructure control.

Other work has exploited the large length scales of colloidal crystals to exert control over defects at the single particle level, falling within the second category of methods of microstructure control. The application of local forces on 2D crystals with optical traps has yielded demonstrations of direct control over individual dislocations and their reactions[45], the topology of grain boundaries[46], and the misorientation angle of a grain boundary loop[47]. Notable limitations of the optical force technique are the difficulty of applying it to 3D systems and the need to locate and image each defect to be manipulated. Besides optical forces, it has also been shown that local forces exerted by active particles can drive microstructure changes. Van der Meer *et al.* have shown for hard-sphere systems in two[48] and three dimensions[49] that the addition of active particles to systems with grain boundaries can result in accelerated kinetics of polycrystalline annealing, resulting in single crystals on short timescales.

Such active particles are but one example of a microscopic 'tool' – a specialized applicator of force designed to achieve target microstructures. In general, tools are specifically designed to enact certain transformations on their working material. Figure 1 schematically illustrates how control of dislocations permits control over the internal structure of a crystal through directed local plastic deformations. We explore how a 'tool-particle' can be designed for manipulation of defects (in this case dislocations) by changing its shape. Given that modern particle synthesis techniques are capable of producing a wide variety of shapes[50–52], we seek a general method of designing the shape of the particle-as-tool for maximum interaction with specific types of dislocations.

Our study uses the linear elastic formalism to understand the interaction between a self-propelled interstitial colloidal particle and dislocation microstructures in a crystal where spherical particles interact *via* steeply repulsive isotropic potentials (*i.e.* nearly hard spheres). The interaction between interstitial and dislocation is estimated and designed by sampling the linear elastic strain fields of both objects. Our work seeks to provide a means to re-configure microstructure after crystallization has already occurred, which allows for the possibility of reconfigurable and responsive colloidal materials with functional defects.

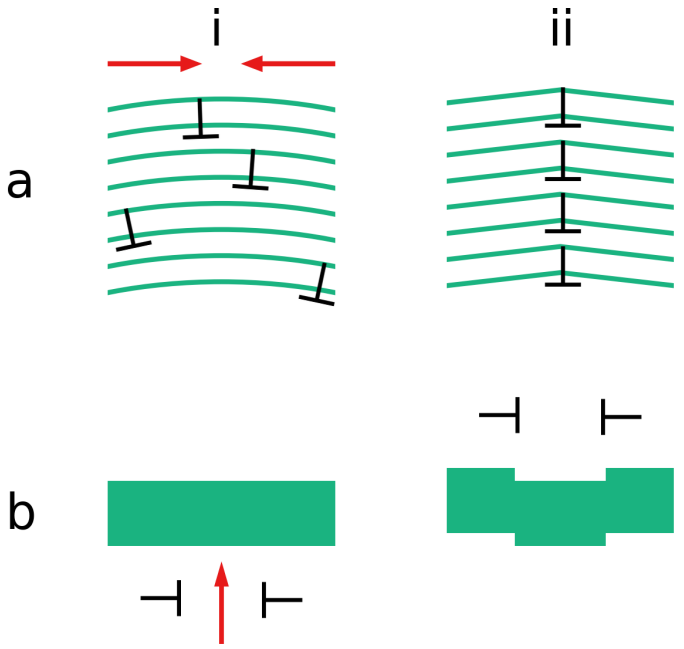

Fig. 1 Examples of how direct control over dislocations can reconfigure crystalline materials. **ai-ii** Bending localization (or grain boundary formation) **ai** dislocations (⊥) are initially distributed randomly, resulting in low, evenly distributed curvature. Forces are applied to dislocations (red arrows). **aii** Dislocations are concentrated, resulting in high local curvature. **bi-ii** Coherent boundary roughening by passage of dislocation dipoles. **bi** Force (red arrow) is applied to a dislocation dipole to drive it towards a coherent grain (green). **bii** After passage through the coherent grain, the dipole has roughened the boundaries with a local shift of one Burgers vector.

In section 2 we describe the model system and methods employed in this study which are standard or introduced elsewhere. In section 3 we apply these methods and introduce new methods created for this study to design interstitial tool particles capable of internally restructuring a colloidal crystal.

2 Model and Methods

To optimize the interaction between an interstitial and a dislocation as a function of interstitial geometry, the strength of the interaction must be measured for each trial geometry. This presents a difficult sampling problem, as thermalized strain fields must be sampled over long time scales and dislocations require large simulation sizes due to their long-range interactions. To address this difficulty, we propose a technique we term 'strain alchemy'. In a typical alchemical simulation[12], the free energy of a system is minimized by allowing some design parameter of the particle interaction to fluctuate as a thermodynamic quantity over the course of the simulation. This procedure results in near-optimal interaction parameters for the target state. Such a tactic involves

making trial changes to an interaction potential, and then sampling system configurations with a molecular dynamics (MD) or Monte-Carlo (MC) simulation[12].

Instead of directly proposing new interstitial shapes, we develop a method in which the strain field produced by the interstitial is allowed to fluctuate. Provided the magnitude of this strain field remains low enough, then linear elastic methods can be used to calculate the free energy of interaction of this field with another – such as that produced by a dislocation. The optimal strain field is then translated into an optimal particle shape. By approximating the objects of interest as strain fields we avoid extensive MD or MC sampling for each trial move. In this study, we develop this strain alchemy algorithm and apply it to the optimization of interstitial-edge dislocation and interstitial-loop dislocation interactions. In the the remainder of this section, we outline the model system and standard simulation techniques employed. Application of these techniques and development of new methods is covered in section 3.

2.1 Interstitial Sites

A face-centered cubic (FCC) crystal of hard spheres at contact contains obstruction-free channels that lie in the $\{111\}$ family of planes along the $\langle 1\bar{1}0\rangle$ family of directions. These are advantageous sites for interacting with gliding dislocations, as these planes and directions comprise the low-energy slip system for this crystal structure. Fig. 2a-b shows a rendering of the interstitial space present in the cubic close-packed crystal.

At finite pressures and temperatures, these channels locally fluctuate in width as particles undergo thermal motion. Lower pressures also lead to an expansion of the structure, increasing the available free space. If a rod of radius equal to the channel radius for hard spheres at contact is inserted into a nearly-hard-sphere crystal at finite pressure and temperature, local strain fields produced around it are negligible in magnitude. Small increases of rod diameter above this minimum will lead to small local strain values. This perturbative relationship between geometry and local strain field magnitude is advantageous for particle design, as it permits the use of linear elastic approximations. Furthermore, the channel geometry limits the height of hopping barriers during interstitial motion. For a spherical interstitial sitting in tetrahedral or octahedral sites in FCC, motion between sites must be accompanied by local lattice strains that (temporarily) far exceed the linear elastic regime. By working within the channels, the maximum strain induced during particle motion can be limited to the maximum strain produced by the particle at rest, and so particle mobility is treatable within the linear elastic framework.

2.2 The Interstitial Particle

In this study our interstitial probe particle of interest is a segmented rod. We wish to impart to this probe enough degrees of freedom to optimize its interaction with a dislocation's strain field. Therefore, the probe is split into segments, each $a/\sqrt{2}$ long (where a is the lattice constant of the host crystal). This is the smallest meaningful distance at which the local strain of the host

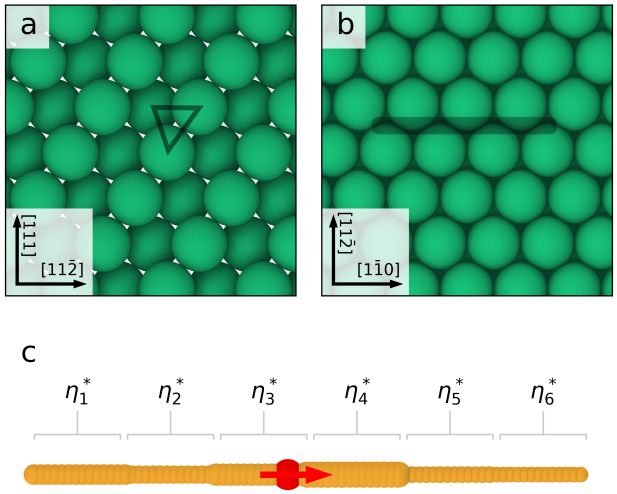

Fig. 2 a A close-packed hard-sphere crystal showing obstruction-free channels aligned with the $\langle 1\bar{1}0\rangle$ family of directions. The triangle highlights the columns of nearest-neighbor particles for the indicated channel. **b** In the here-depicted (111) plane of densely packed spheres, these channels correspond to troughs with triangular cross section, indicated by the shaded rectangle. **c** The probe particle model. Rigid-body segments (yellow) with repulsive interactions are rendered at the zero-energy isosurface. The center particle of the rigid body (red) coincides with the particle's center of mass. The mass, center of mass, and moment of inertia of the probe are calculated as though it is comprised of overlapping spheres of the same density as the lattice particles. A force (red arrow) is applied along the probe axis. The probe shown is one example of a sequence of segment diameters.

lattice can be measured, and yields 'internal' degrees of freedom for the probe equal to one value (the strain magnitude η^*) for each segment. These segments are allowed to change independently during optimization. Beyond internal degrees of freedom, the probe's position relative to the dislocation core can also be changed: it can be placed in any of the channels present in the $\{111\}$ family plane parallel to the $\langle 1\bar{1}0\rangle$ family of directions (indicated in Fig. 2b). Fig. 2c shows a schematic of the rod geometry used in MD simulations (See section 2.4 for MD methods).

2.3 The Method of Eigenstrains

To predict the strain field surrounding an interstitial we employ the method of eigenstrains[53]. Each segment of the interstitial probe will be represented by a single strain value. These strains can be called 'non-elastic' because they arise from displacements of particles by the interstitial, not by a stress field. Adopting Mura's terminology, we refer to these strains as 'eigenstrains'. The total strain (ε_{ij}) in the system is taken to be the sum of the non-elastic eigenstrain (η^*_{ij}) and the elastic strain (η_{ij}). For a continuum material at rest, the relation $\varepsilon_{ij} = \frac{1}{2}\left(\frac{\partial u_i}{\partial x_j} + \frac{\partial u_j}{\partial x_i}\right)$ holds (where $\vec{u}$ is the displacement vector and $\vec{x}$ is the position vector). This relationship between strains and displacements is known as 'compatibility'. Such a relationship allows the elastic deformation η_{ij} to be found for arbitrary eigenstrains. In this work we employ

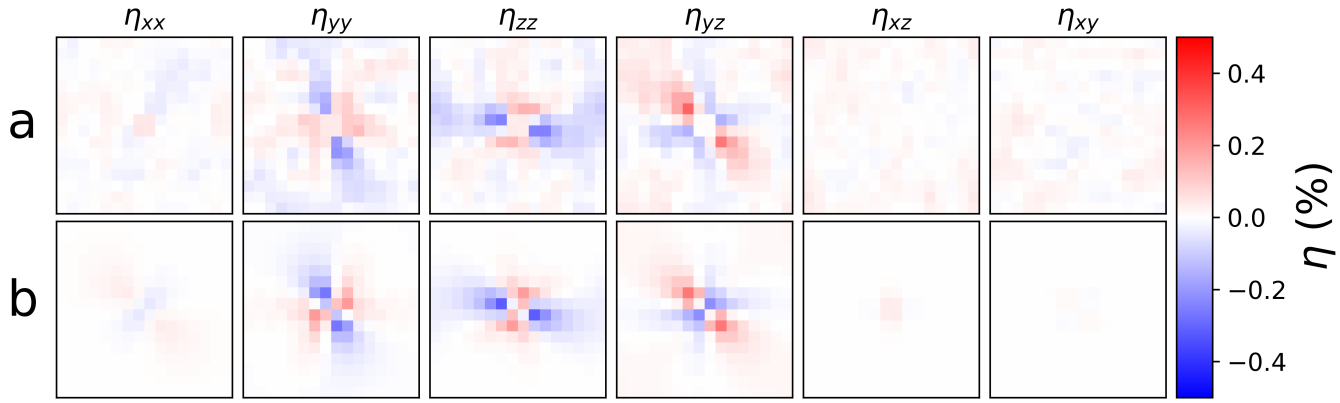

Fig. 3 Comparison of sampled **a** and predicted **b** strain fields for a segmented rod interstitial. A single slice of the strain field is shown through the midpoint of the probe, with the long axis normal to the image plane. The sampled and predicted field show good agreement overall with only minor differences for regions in closest contact with the interstitial.

an implementation of the Fourier transform method of computing total strain distributions from eigenstrains based on the equations presented by Mura[53] and validated against analytic solutions for inclusions derived by Chiu[54]. The elastic strain field found in this way can be directly connected to the deformation free energy of the material in the small strain limit[55].

When considering a rod-like interstitial at rest in the $\langle 1\bar{1}0\rangle$ aligned channels of the FCC structure (section 2.1), an increase in interstitial diameter does not produce a purely dilatory displacement of nearest neighbors. This is because (unlike for tetrahedral or octahedral interstitial sites) all neighbors of the $\langle 1\bar{1}0\rangle$ channels are not equidistant from the channel center. The correct relation between probe diameter and channel neighbor displacements (i.e. eigenstrain) was found semi-analytically. An eigenstrain matrix was found (algebraically) which displaced the nearest neighbors of the close-packed channel sufficient to clear enough space to fit a probe of given diameter. A corrective scaling factor was required to match the eigenstrain sampled from simulations of uniform diameter probes to this derived eigenstrain matrix. The scaling factor is needed because the derived eigenstrains where found from the close-packed FCC crystal geometry, and the simulations are conducted at finite pressures and temperatures. See SI for additional information about the accuracy of these strain predictions †.

2.4 Molecular Dynamics Methods

All MD simulations reported here are performed with `HOOMD-blue`[56,57]. In simulations of dislocations, all lattice particles interact *via* the shifted-Weeks-Chandler-Andersen potential[58] (SWCA), whereby the origin is shifted to the surface of the particle. The value of σ used in this potential was set to 0.07, and the potential was shifted in radius so that the minimum (located at $\sigma 2^{1/6}$ in the unshifted case) is at a distance of $2^{1/6}$. In this work we will refer to the diameter of the host particles as D, which is equal to $2^{1/6}$. Simulations were carried out in the NPT ensemble *via* equations derived by Martyna *et al.*[59]. System thermal energy was held at $kT = 0.1$, pressure at $P = 2$, and particle mass was fixed at $m = 10$ (in simulation units). This choice of parameters yields a crystal with an acceptably large range of linear elastic behavior[60]. The elastic modulus tensor was sampled *via* fluctuations of the system box parameters and stress tensor[61].

Stain-field representations of line and loop dislocations were sampled from MD simulations. Dislocation line arrays were created by subtraction of a half plane of particles in a simulation box spanning 60 unit cell lengths in the x direction (aligned with crystal direction $[1\bar{1}0]$), 24 unit cell lengths in the y direction (aligned with crystal direction $[11\bar{2}]$), and 20 unit cell lengths in the z direction (aligned with crystal direction $[111]$). Particles within a rectangle spanning one Burgers vector in the x direction, the full box width in the y direction, and half the box height in the z direction were deleted from an initially perfect crystalline domain. The crystal in between the top and bottom of the deleted rectangle was then stretched in the x direction, so that the gap was closed. Upon MD simulation, this initial configuration rapidly equilibrated into two partial dislocation pairs, with glide planes separated by one half of the height of the simulation domain. See SI for a diagram of dislocation preparation †. Box boundary conditions are all periodic, and the final particle count was 346,992. Per-particle strain fields were collected from 100 decorrelated samples, and a voxelized representation was created by binning. Bins form an isotropic grid with orthogonal distance $a/\sqrt{2}$ between bin centers. The final line-dislocation strain tensor has size $139 \times 32 \times 56 \times 3 \times 3$.

Due to the compact size of the dislocation loop, we used a smaller simulated domain without strong loop-loop interactions across the periodic boundary conditions. The simulation contained a crystal domain of the same orientation as used for line dislocations but containing $30 \times 20 \times 16$ unit cell lengths in the x, y, and z box directions (corresponding to $[1\bar{1}0], [11\bar{2}], [111]$ crystal directions, respectively). The extrinsic loop was created by the addition of a parallelogram of particles 1 plane thick in the x direction and 3 particles wide and tall. To make room for the extra particles, a section of the initially perfect crystalline

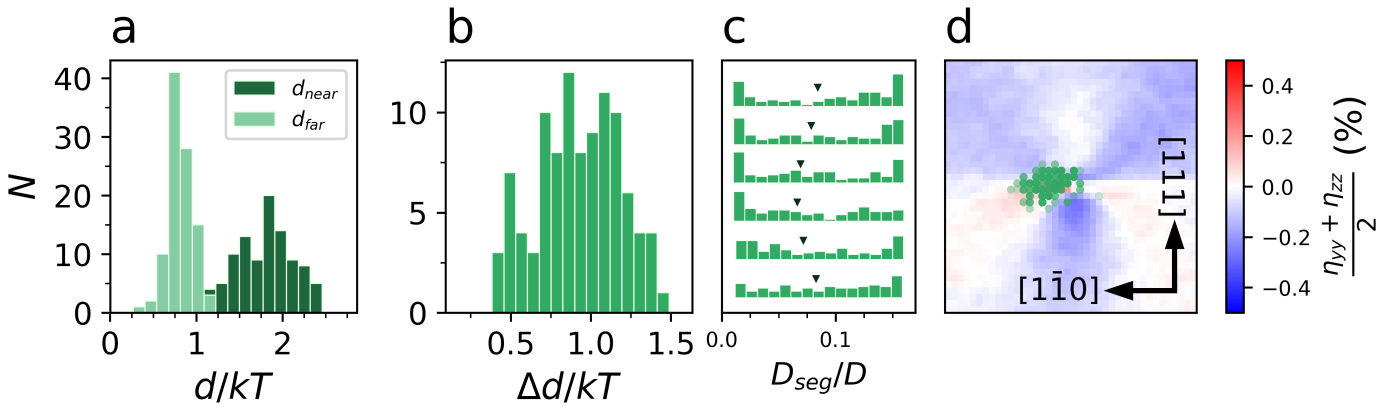

Fig. 4 The aggregated results of 100 MC solver runs on an edge dislocation. **a** Histogram of the barriers estimated from the eigenstrain procedure. **b** Distribution of solution fitness, as defined by the difference of barriers near and far from the dislocation. **c** Histograms of the diameters of each of the six segments that comprise the probe. The mean of each distribution is indicated with a chevron. **d** Location of final solution position, relative to dislocation core.

domain bounded by the glide tube of the dislocation loop was compressed along the x direction, which opened up a gap in the center of the simulation domain. An extra half plane of particles was then inserted into this gap. Upon MD simulation, this initial configuration rapidly equilibrated into a dislocation loop. See SI for a diagram of dislocation preparation †. The total lattice particle number after loop formation was 115,209. The strain field surrounding a loop was sampled in the same manner as the line dislocation, yielding a loop dislocation strain tensor of size $69 \times 40 \times 45 \times 3 \times 3$.

In all cases the segmented probe is simulated as a collection of isotropic repulsive potentials (interacting *via* the same SWCA potential as the lattice particles). To produce variations in segment diameter, the radial shifting of the SWCA potential is varied accordingly. Relative positions are maintained and torques handled during MD integration by rigid-body simulation[62].

3 Results

3.1 Interstitial Particle Strain Field Mapping

Since we use the strain field produced by the interstitial to estimate interaction energies and probe mobilities, it is important that the analytically predicted field is sufficiently accurate. Fig. 3 shows a slice through the center of the strain field surrounding a probe of constant radius. The MD sampled field (3a) and analytically predicted field (3b) show good agreement in distribution and magnitude for regions not in direct contact with the interstitial. In these plots, one pixel corresponds to a region of crystal $a/\sqrt{2}$ per side. As segment radius is increased, eventually significant differences in strain magnitude arise between the predicted and sampled fields. This is because the methods employed here are only applicable in the small-strain (linear elastic) limit. When the radii of probe segments are permitted to fluctuate, an upper limit is used to restrict the search to the linear regime (see SI for details †).

3.2 Interaction Estimation *via* Interstitial Mobility Estimation

With the ability to map the strain field of a segmented probe particle to its geometry, the path is clear to use a Monte-Carlo (MC) style optimization scheme to maximize the interaction free-energy between the rod and another strain-field-producing object (such as a dislocation). Within the linear elastic approximation, linear superpositions of fields are also valid fields. Therefore, the strain field of the rod under design can be superimposed with the strain field of a dislocation and the total strain field energy evaluated according to the expression[55]:

$$F_{elastic} = \int_{\vec{r}} \frac{V}{2} \sum_{ijkl} C_{ijkl}\eta_{ij}(\vec{r})\eta_{kl}(\vec{r}), \quad (1)$$

where $\eta(\vec{r})$ is the strain tensor describing a volume V centered at position $\vec{r}$. Here the tensor field η is the sum of two tensor fields, one representing the probe and one the dislocation. C_{ijkl} is the elastic modulus tensor. By comparison to the strain-field energy of both fields widely separated, interaction energies as a function of relative position can be determined.

Before optimization, a likely guess as to what kind of strain field maximizes the interaction between a segmented probe and a dislocation is straightforward: larger probe strains will always increase repulsive interaction strength, while fields that result in total cancellation of the dislocation's field will likely maximize attractive interactions. However, we are not concerned here only with the interaction strength, but also the mobility of the probe. In order for an active interstitial to interact with a dislocation, it must have sufficient mobility to move through the defect-free crystal. Upon encountering a dislocation, the desired behavior is to then become bound, unable to escape from the vicinity of the defect. If we assume that particle migration through the crystal is achieved by hopping through a periodic free-energy surface (with the periodicity defined by the geometry of the crystal in the direction of travel), then we seek an interstitial with location-dependent barrier height (d). Far from the dislocation, the barrier (d_{far}) should be as low as possible, while the barrier in the

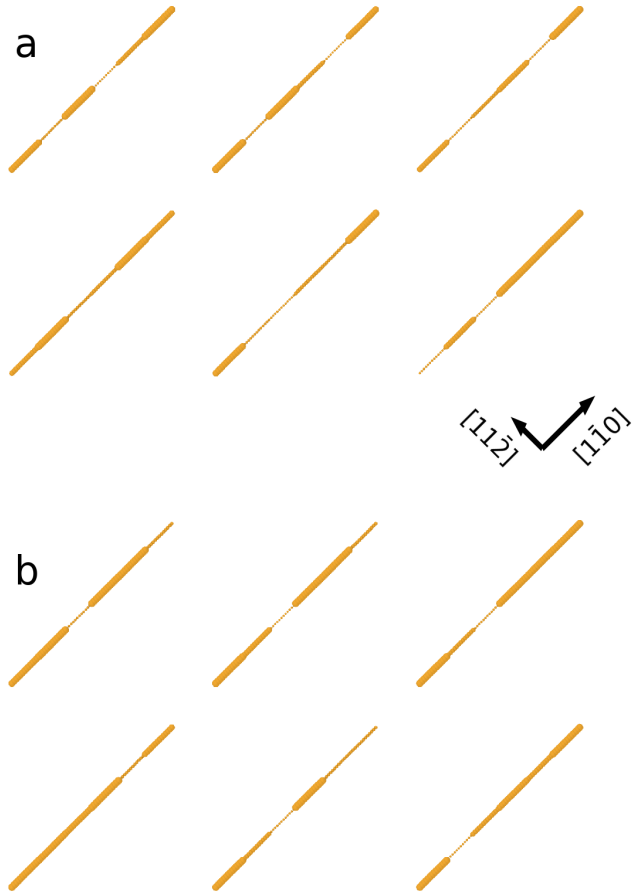

Fig. 5 Renderings of the top six optimized probes for interacting with an edge dislocation (**a**) and extrinsic dislocation loop (**b**). The surface rendered is the zero-energy isosurface of the SWCA potential. Directions relative to the rod when placed in the host crystal are noted. The average line direction of Shockley partials is parallel to $[11\bar{2}]$.

vicinity of the defect (d_{near}) should be as large as possible. Consequently, we seek a particle geometry optimization which takes into account the free-energy barrier that limits probe mobility. We expect both d_{far} and d_{near} to increase with an increase in probe strain, which means that high mobility and strong defect interaction are competing design goals.

It is possible to estimate this barrier height from the strain field that surrounds a segmented probe interstitial (which can be rapidly predicted using the method of eigenstrains). This method of approximation relies on the special geometry of the segmented probe particle: because each segment imposes local strains that are within the linear regime, there will be no high-strain intermediate states as the probe hops from one site to the next. The barrier to probe movement then arises due to the strain free-energy that is dissipated in each hop. As the probe approaches new volumes of the pristine crystal, it imposes strain, which increases the local free energy. Simultaneously, regions from which the rod leaves relax their local strain free energy. This relaxed free-energy is not recaptured by the rod, but instead escapes as heat. Therefore the hopping of an interstitial rod requires that new strain energy be stored in volumes ahead of the particle motion, while previously stored strain free energy is not recovered. This is the source of resistance to motion. The value of this hopping barrier can be calculated from a given strain field according to Eq. 2:

$$
\begin{aligned}
d &= \sum_{\vec{r}} ||F_2(\vec{r}) - F_1(\vec{r})|| \\
F_1(\vec{r}) &= \frac{V}{2} \sum_{ijkl} C_{ijkl} \left[\eta^D(\vec{r}) + \eta^I(\vec{r})\right]_{ij} \\
&\qquad \times \left[\eta^D(\vec{r}) + \eta^I(\vec{r})\right]_{kl} \\
F_2(\vec{r}) &= \frac{V}{2} \sum_{ijkl} C_{ijkl} \left[\eta^D(\vec{r}) + \eta^I(\vec{r}+d\vec{r})\right]_{ij} \\
&\qquad \times \left[\eta^D(\vec{r}) + \eta^I(\vec{r}+d\vec{r})\right]_{kl}
\end{aligned}
\tag{2}
$$

with C_{ijkl} being the crystal's elastic modulus, V is the volume of an element centered at $\vec{r}$, η^D the strain field of the dislocation, and η^R the strain field of the segmented probe interstitial.

3.3 Strain Field Monte-Carlo Algorithm

The optimization of probe-dislocation strain-field-mediated interaction is carried out through a Monte-Carlo style algorithm we developed for this work. The domain of optimization is a voxelized grid, represented by an $n \times m \times o \times 3 \times 3$ tensor, where each point of an $n \times m \times o$ grid (representing the physical dimensions of the optimization area) has a 3×3 local strain tensor. The optimization requires two such tensors: a background tensor, encoding the local strain surrounding a dislocation or other object of interest, and the design tensor, which encodes the values of local strain produced by the probe interstitial. The background tensor's values and size are set by a voxelization procedure used to measure time-averaged local strain in an MD simulation, described elsewhere[60]. The design tensor is used in two forms: the eigenstrain and strain representations. These forms are related through the method of eigenstrains[53]. Changes to the segmented probe interstitial's geometry are represented through changes to the eigenstrain design tensor, which is then converted into the strain representation before evaluation is carried out. Since the conversion from eigenstrain representation to strain representation is the limiting step, and the extent of the strain field of the segmented rod interstitial is much smaller than the sampling of the dislocation's strain field, the design tensor can have fewer elements (cover a smaller volume) than the background tensor. The steps in choosing a strain configuration and evaluating its fitness are as follows:

1. Select a segment of the probe and assign a new diameter value to it.

2. Set the elements of the eigenstrain design tensor that cor-

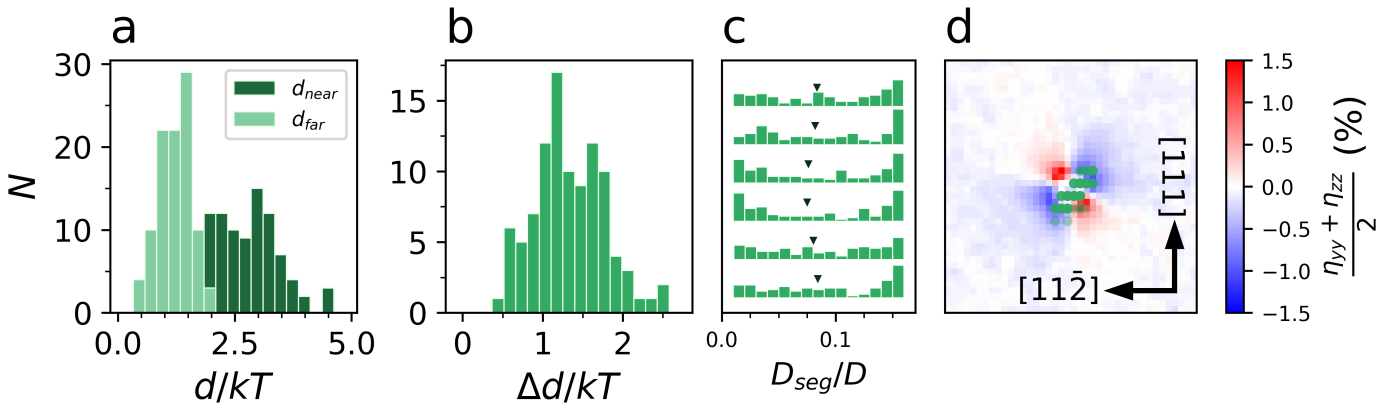

Fig. 6 The aggregated results of 100 MC solver runs on an extrinsic dislocation loop. **a** Histogram of the barriers estimated from the eigenstrain procedure. **b** Distribution of solution fitness, as defined by the difference of barriers near and far from the dislocation. **c** Histograms of the diameters of each of the six segments that comprise the probe. The mean of each distribution is indicated with a chevron. **d** Location of final solution position, relative to dislocation loop center axis.

respond to this probe segment to values which describe the displacement caused by this diameter.

3. Compute the strain representation of the design tensor with the method of eigenstrains.

4. Shift (with edge wrapping) the strain design tensor so that the probe origin is near the dislocation core and evaluate the hopping barrier, d_{near}.

5. Shift (with edge wrapping) the strain design tensor so that the probe origin is at a location far from the dislocation core. Compute the estimate of the hopping barrier d_{far}.

6. Calculate the fitness of the design tensor as $f = d_{\text{near}} - d_{\text{far}}$.

7. Accept the new design tensor with probability $e^{(f-f_0)/kT_{\text{alch}}}$, where f_0 is the fitness of the previously accepted design tensor, and kT_{alch} is a thermal energy that can be lowered over the course of the optimization to restrict the magnitude of strain field fluctuations.

8. Repeat until convergence (or until kT_{alch} is reduced to a negligible value).

The sampling of d_{near} and d_{far} depends strongly on the position of the probe relative to the glide plane. To avoid introducing assumptions concerning which location will produce the fittest solution, changes to the position of the probe can also be included in the MC procedure. For this study positional moves are made less often than strain moves.

3.4 Use Case: Line Dislocations

Using the procedure outlined in section 3.3, the interaction of a segmented probe interstitial and a line dislocation of pure edge character was performed (see section 2.4 for details). The eigenstrain representation of the particle is comprised of 6 coupled blocks of 4 voxels each, centered in the design tensor. The number of blocks represents segments of the probe. 6 was chosen as the number of segments to avoid excessively high aspect ratios. Segment radii are permitted to approach 0, effectively shortening the probe if advantageous for optimization. The size of the design tensor was sufficient for strain fields to decay to negligible values at the edges of the domain.

Fig. 4 shows summary information from 100 MC trials preformed on line-dislocation arrays (See SI for solver parameter details†). The final locations that maximize interaction (shown in Fig. 4d) are clustered on the leading edge of the dislocation, near the tensile lobe associated with the η_{zz} field. Fig. 4c shows histograms of the segment geometries. The distributions are broad, however mean values display a clear trend of high values at the probe ends, and low values at the center. This dog-bone configuration appears to maximize the probe's escape barrier when near a lobe of the dislocation's η_{zz} field. The top six highest fitness solutions are shown in Fig. 5a. Aside from the average trends of high diameter ends and low diameter middles, some high-fitness geometries also have a large diameter central segment, resulting in a serrated appearance. This appears to be a further refinement of the average trend.

3.5 Use Case: Dislocation Loops

The same MC procedure (section 3.3) as for line-edge dislocations (section 3.4) was applied to extrinsic dislocation loops (see section 2.4 for details). Fig. 6 summarizes the results of 100 MC trials on the sampled loop strain data. The higher values of mobility barriers in the neighborhood of the dislocation loop immediately become clear. The strain fields perpendicular to the loop glide axis are higher in magnitude than those surrounding a line-edge dislocation. The line dislocation has negligible strain values in the direction parallel to the line vector; most strain energy is contained in the field parallel to the glide direction. The bending of the dislocation-loop lines produces a more highly strained local environment for the probe to interact with. The locations of maximum interaction are distributed within the area of the loop. There is a preference for the compressive corners of the loop over

the tensile corners. The histogram of segment diameters reveals large populations of high and low diameters (and a relative lack of intermediate diameters), with almost no pattern to how these segments are ordered. Fig. 5b shows the top six solutions of optimal probe shape, highlighting again that the key feature for optimal interaction is a low-strain segment surrounded by large-strain segments. There seems to be no strong preference for where on the probe the small segment is placed.

3.6 MD Validation of Barrier Estimation

To test the validity of estimating hopping barriers from predicted strain fields (section 3.2), the optimized probes found in sections 3.4 and 3.5 were placed within a defect-free FCC crystal domain and a force was applied that aligned with the rod's axis. Several hydrostatic strains were applied to the simulated crystal in order to test the rod's mobility in different strain environments. Fig. 7a shows the average velocity of the rod under different magnitudes of force ($\vec{f}$) for different hydrostatic strain conditions. Curves are fit to the velocity data using the Fokker-Planck equation solution for a periodic 1D potential[63]. Two free parameters—the barrier height (d_{fit}) and the damping constant (γ)—were used for the fit. Barrier heights were compared to those found from the optimization process (d_{eig}). Fig. 7b shows the comparison of the estimated and fit barrier height. The fit and predicted values have a constant offset, but are otherwise related linearly with a proportionality constant close to unity. The origin of the offset is unknown, but may be a product of the fluctuating probe orientation and thermal bending of the interstitial channels, which are effects neglected by the estimation method. The value of γ found by fitting is related linearly to the pressure of the crystal (see Fig. 7). This trend in γ reveals that strained environments can change the frequency of collisions between the interstitial and the crystal particles, which is an expected result. In optimization of the probe geometry, this γ effect can be neglected, since it is predominantly important at high forces. Additionally, since γ is positively linearly correlated with d, both parameters need not be considered to maximize differences in average particle velocity.

3.7 MD Simulation of Interstitial-Dislocation Interaction

To test the validity of the solutions (sections 3.4 and 3.5) produced by the MC optimizer, MD simulations were performed. The optimized probe particle was placed within the simulated crystal (the same geometry as was created for sampling of the defect strain fields) at the location of maximum interaction found by the optimization, with a force applied to the rod along its long axis. Fig. 8a shows the relationship between the distance traveled by the optimized probe, and the slip between a pair of tagged tracers positioned on either side of the dislocation slip plane. On this plot, a slope of 1 indicates that the dislocation and the optimized probe are traveling together, producing one Burgers vector of slip per full transit of the periodic box by an optimized probe. As the force exerted by the interstitial is increased, the total distance traveled by the dislocation and the probe increases. The inset in Fig. 8a shows the velocity of the probe as a function of force. A local velocity maximum near $f \simeq 9.0$ is observed. For $f > 16.8$ the

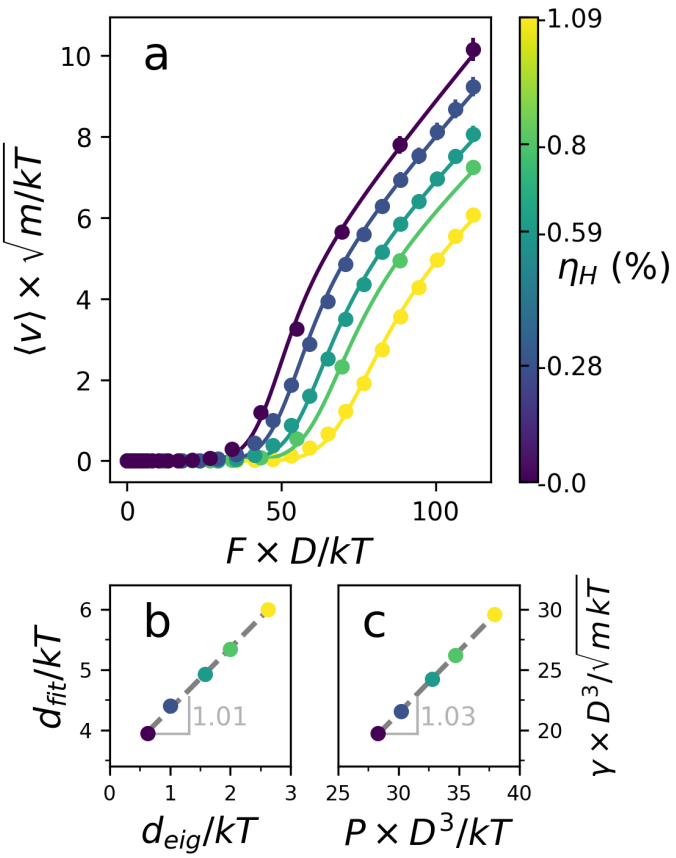

Fig. 7 a Probe interstitial velocity as a function of force for various conditions of hydrostatic strain. Curves are fit as functions of γ and barrier height, d_{fit}. **b** Relationship between the fitted value of d and that predicted by the eigenstrain estimate. **c** Relationship between the fit value of γ and pressure. The quantity $\gamma \cdot D^2$ scales linearly with applied system pressure.

probe becomes completely unbounded from the dislocation. The dislocation array stops moving unidirectionally and the probe's velocity as a function of force becomes monotonic. Fig. 8b-e shows renderings of simulations where the probe particle is interacting with a partial edge dislocation line. Also shown is a slice of the simulation domain before and after the dislocation array was driven to glide across the periodic box several times. The central segment of the crystal can be seen to have slipped past the remainder of the system. This slip increases by one full Burgers vector magnitude for each time that the partial dislocation pair transits the periodic simulation domain in the $[1\bar{1}0]$ crystal direction.

The same study and analysis was also conducted for the dislocation-loop-optimized probe. In this case one of the tagged tracer particles was placed within the glide cylinder of the tube. Fig. 9a shows the correlation of optimized probe travel and loop travel as a function of force. As these simulations were run for the same amount of time as the line dislocation tests, it is clear that the mobility of the loop-probe pair is much higher. The striking difference in mobility for loop and line dislocations is not surprising, as loops contain a much shorter length of dislocation line

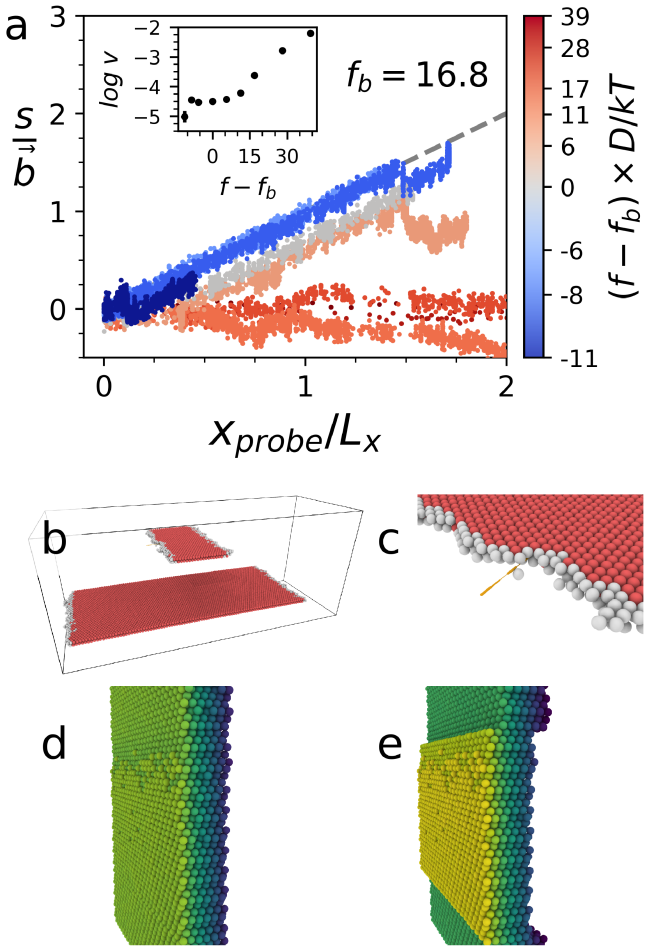

Fig. 8 a Optimized probe distance traveled versus slip of the central region for a simulated edge dislocation array. Particle forces above $f_b = 16.8$ result in small slopes, indicating that the active particle escapes from the vicinity of the dislocation. The inset shows the velocity of the optimized probe as a function of force. There is a local maximum in velocity before the breakaway force. Snapshots of the optimized probe as it interacts with a partial edge dislocation, rendered with OVITO[64]. **b** The dislocation array, shown with all particles having an FCC-like neighbor shell removed. The red particles are members of the stacking faulted layer and the white particles are members of the disordered core. **c** Close-up of the optimized particle as it interacts with one of the partial dislocations. **d** A slab of particles at the start of the simulation, color coded by x position. **e** The same particles after several passages of the dislocation array through the box.

that has to glide. In the simulations shown here, the length of Shockley dislocations present in the loops is $\sim 18a$ (with the total length of all dislocations $\sim 30a$), while line dislocation simulations contained only Shockley partials spanning $\sim 120a$. The escape force for the loop optimized probe is larger than that for the line dislocation, above $f \simeq 29.2$. The probe's velocity (Fig. 9a inset) as a function of applied force shows similar features to the line dislocation case, however the local maximum ($f = 16.8$) and minimum ($f = 29.2$) are more distinct. The increased force value of the maximum and minimum is consistent with the higher Δd achieved for the optimization of the loop probe. Fig. 9b-e shows images of the simulated loop-active particle system. Fig. 9c shows the dislocation lines present in the extrinsic loop, as found with the DXA algorithm[65] implemented in OVITO[64]. The loop structure is comprised of three dislocation types: partial (Shockley) dislocations, forming the two ends of the dissociated dislocation loop tube, as well as stair-rod dislocations and Hirth dislocations at the corners of the loop, with line directions parallel to the glide axis of the loop. Similar to the case of the line dislocation array, multiple transits of the dislocation loop through the simulation cause slip of the regions bounded by the glide cylinder.

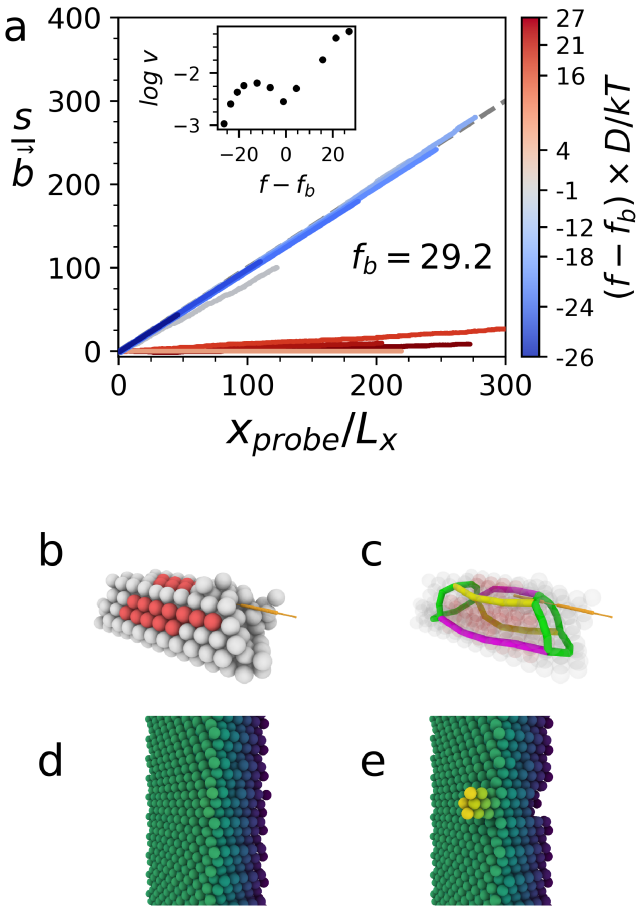

Fig. 9 a Optimized probe distance traveled versus slip of the loop glide cylinder region for a simulated extrinsic dislocation loop. Probe forces above $f_b = 29.2$ result in small slopes, indicating that the active probe escapes from the vicinity of the dislocation. Inset shows the velocity of the probe as a function of force. Snapshots of a segmented rod interstitial particle as it interacts with an extrinsic dislocation loop, rendered with OVITO[64]. **b** Close-up of the dislocation loop structure with optimized probe nearby. Particles with FCC-like environments have been removed for visibility. Red particles are members of stacking faults, and white particles have disturbed neighbor shells. **c** Close-up with particles rendered transparently and dislocation lines highlighted: green lines are partial (Shockley) dislocations ($\vec{b} = \frac{1}{6}\langle 112 \rangle$), purple lines are stair-rod dislocations ($\vec{b} = \frac{1}{6}\langle 110 \rangle$), and yellow lines are Hirth dislocations ($\vec{b} = \frac{1}{3}\langle 001 \rangle$). **d** A slab of particles at the beginning of the simulation, colored by x position. **e** The same particles after several transits of the loop through the box.

The straight partial dislocations simulated in this study cross the periodic box boundaries, and so can be thought of as infinite in extent. Therefore, it is best to compare the performance of probes interacting with line and loop dislocations on a per-length basis. In a periodic box containing one probe particle and two straight edge dislocations that have decomposed into four Shockley partials, the breakaway force of the line dislocation optimized probe is $f/l \simeq 16.8/120a = 0.14/a$. If in the loop dislocation case we consider only the Shockley partial length, then the loop dislocation optimized breakaway force per unit length is $f/l \simeq 29.2/18a = 1.62/a$. The large difference in breakaway force on a per unit length basis emphasizes the increased coupling between a curved dislocation and the probe interstitial.

The probe interstitial can only interact *via* its strain field in a small volume (the volume of non-negligible strains produced by the probe). Ultimately, the small size of the probe results in strain fields that rapidly decrease in magnitude with distance, much like a point source. A bent dislocation, like those in a small loop, can fit more dislocation line length within range of the probe's strain field. In fact, the straight dislocation case can be compared to a very large diameter loop, which on length scales similar to the range of the probe's strain field appears straight. The results presented here show that as the circumference of a dislocation loop is scaled from $\simeq 9a$ to $\simeq 60a$, a greater than ten-fold reduction in optimal probe binding strength per unit length occurs due to the reduction of dislocation curvature. An implication of this result is that dislocation bends or jogs, which have locally high curvature should also be expected to strongly interact with the same probes that strongly interact with small dislocation loops.

4 Conclusion

We have shown that there is a robust mapping between the geometry of a repulsive segmented probe particle embedded as an interstitial in an FCC crystal of repulsive spheres and the local strain field that is produced around it. We exploited this predictive connection to allow the use of MC methods to design the nature of the interaction between the interstitial probe and other strain-field-producing disturbances in the crystal. We have also shown that the mobility of such an interstitial is well-approximated through consideration of the strain field alone, and that by placing constraints on the mobility of the interstitial in different local environments (*i.e.*, near to and far from a dislocation), the interaction between this interstitial and another object can be tuned. A striking feature of this design method is its computational efficiency. The simple Python implementation of the MC solver used here requires approximately one day per solution to run on a single CPU. In contrast, each trial force MD simulation of the line dislocation arrays requires a full week of NVIDIA® Tesla® P100 GPU time. If every trial geometry, position, and force required such a simulation for evaluation, then it would be unfeasible to carry out this scheme.

This work demonstrates a route towards microstructure control in colloidal materials through a designed, active tool particle interstitial that can manipulate internal defects. Currently, the most powerful tool for 3D microstructure creation available to colloidal scientists is templating, whereby the boundary conditions of crystallization are changed to favor the creation of desired defects. Our work complements such efforts by providing a means to reconfigure microstructure *after crystallization has already occurred*, which opens the possibility for colloidal crystal mechanical and optical devices. Furthermore, increasing defect mobility by interaction with active interstitial probes is a route to lowering colloidal crystal defect quantity. Active particles designed in this way can be used to 'sweep out' undesired defects and microstructures. This work demonstrates a colloidal microstructure control scheme that exploits the designability of colloidal crystal subunits in a way not achievable with atomic materials.

Conflicts of interest

There are no conflicts to declare.

Acknowledgments

This material is based upon work supported by the U.S. Department of Energy, Office of Science, Basic Energy Sciences, under Award Number DE-SC0013562. This research utilized computational resources and services supported by Advanced Research Computing at the University of Michigan, Ann Arbor, and used the Extreme Science and Engineering Discovery Environment (XSEDE), which is supported by National Science Foundation Grant ACI-1053575 (XSEDE Award DMR 140129). We thank Dr. J. Dshemuchadse and Dr. L. Qi for helpful discussions.

Notes and references

1 K. P. Velikov, C. G. Christova, R. P. A. Dullens and A. v. Blaaderen, *Science*, 2002, **296**, 106–109.
2 M. E. Leunissen, C. G. Christova, A.-P. Hynninen, C. P. Royall, A. I. Campbell, A. Imhof, M. Dijkstra, R. v. Roij and A. v. Blaaderen, *Nature*, 2005, **437**, 235.
3 S. C. Glotzer and M. J. Solomon, *Nature Materials*, 2007, **6**, 557.
4 D. Nykypanchuk, M. M. Maye, D. v. d. Lelie and O. Gang, *Nature*, 2008, **451**, 549.
5 A. Haji-Akbari, M. Engel, A. S. Keys, X. Zheng, R. G. Petschek, P. Palffy-Muhoray and S. C. Glotzer, *Nature*, 2009, **462**, 773–777.
6 Q. Chen, S. C. Bae and S. Granick, *Nature*, 2011, **469**, 381.
7 K. Miszta, J. de Graaf, G. Bertoni, D. Dorfs, R. Brescia, S. Marras, L. Ceseracciu, R. Cingolani, R. van Roij, M. Dijkstra and L. Manna, *Nature Materials*, 2011, **10**, 872–876.
8 P. F. Damasceno, M. Engel and S. C. Glotzer, *Science*, 2012, **337**, 453–457.
9 Y. Zhang, F. Lu, K. G. Yager, D. v. d. Lelie and O. Gang, *Nature Nanotechnology*, 2013, **8**, 865.
10 T. Vissers, Z. Preisler, F. Smallenburg, M. Dijkstra and F. Sciortino, *The Journal of Chemical Physics*, 2013, **138**, 164505.
11 Y. Wang, Y. Wang, X. Zheng, É. Ducrot, J. S. Yodh, M. Weck and D. J. Pine, *Nature Communications*, 2015, **6**, 7253.
12 G. van Anders, D. Klotsa, A. S. Karas, P. M. Dodd and S. C. Glotzer, *ACS Nano*, 2015, **9**, 9542–9553.

13 É. Ducrot, M. He, G.-R. Yi and D. J. Pine, *Nature Materials*, 2017, **16**, 652.

14 H. Lin, S. Lee, L. Sun, M. Spellings, M. Engel, S. C. Glotzer and C. A. Mirkin, *Science*, 2017, **355**, 931–935.

15 E. Yablonovitch, *Physical Review Letters*, 1987, **58**, 2059–2062.

16 E. Yablonovitch, T. J. Gmitter and K. M. Leung, *Physical Review Letters*, 1991, **67**, 2295–2298.

17 M. Maldovan and E. L. Thomas, *Nature Materials*, 2004, **3**, 593.

18 K. M. Ho, C. T. Chan and C. M. Soukoulis, *Physical Review Letters*, 1990, **65**, 3152–3155.

19 Y. Kim, R. J. Macfarlane, M. R. Jones and C. A. Mirkin, *Science*, 2016, **351**, 579–582.

20 K. V. Tretiakov and K. W. Wojciechowski, *physica status solidi (b)*, 2014, **251**, 383–387.

21 E. Zaccarelli, G. Foffi, K. A. Dawson, F. Sciortino and P. Tartaglia, *Physical Review E*, 2001, **63**, 031501.

22 A. Zaccone, H. Wu and E. Del Gado, *Physical Review Letters*, 2009, **103**, 208301.

23 T. H. Courtney, *Mechanical Behavior of Materials: Second Edition*, Waveland Press, 2005.

24 L. Lu, Y. Shen, X. Chen, L. Qian and K. Lu, *Science*, 2004, **304**, 422–426.

25 S. Noda, A. Chutinan and M. Imada, *Nature*, 2000, **407**, 608–610.

26 O. Painter, R. K. Lee, A. Scherer, A. Yariv, J. D. O'Brien, P. D. Dapkus and I. Kim, *Science*, 1999, **284**, 1819–1821.

27 Y. Akahane, T. Asano, B.-S. Song and S. Noda, *Nature*, 2003, **425**, 944–947.

28 P. W. Voorhees, *Journal of Statistical Physics*, 1985, **38**, 231–252.

29 M. E. Fine, *Metallurgical Transactions A*, 1975, **6**, 625.

30 J. W. Cahn, *The Journal of Chemical Physics*, 1965, **42**, 93–99.

31 J. W. Matthews and A. E. Blakeslee, *Journal of Crystal Growth*, 1974, **27**, 118–125.

32 P. Bellon, *Physical Review Letters*, 1998, **81**, 4176–4179.

33 R. A. Enrique and P. Bellon, *Physical Review B*, 2001, **63**, 134111.

34 A. C. Lund and C. A. Schuh, *Physical Review Letters*, 2003, **91**, 235505.

35 A. R. Bausch, M. J. Bowick, A. Cacciuto, A. D. Dinsmore, M. F. Hsu, D. R. Nelson, M. G. Nikolaides, A. Travesset and D. A. Weitz, *Science*, 2003, **299**, 1716–1718.

36 K. H. Nagamanasa, S. Gokhale, R. Ganapathy and A. K. Sood, *Proceedings of the National Academy of Sciences of the United States of America*, 2011, **108**, 11323–11326.

37 V. W. A. d. Villeneuve, R. P. A. Dullens, D. G. A. L. Aarts, E. Groeneveld, J. H. Scherff, W. K. Kegel and H. N. W. Lekkerkerker, *Science*, 2005, **309**, 1231–1233.

38 B. van der Meer, M. Dijkstra and L. Filion, *The Journal of Chemical Physics*, 2017, **146**, 244905.

39 P. Schall, I. Cohen, D. A. Weitz and F. Spaepen, *Science*, 2004, **305**, 1944–1948.

40 P. Schall, I. Cohen, D. A. Weitz and F. Spaepen, *Nature*, 2006, **440**, 319–323.

41 S. J. Gerbode, S. H. Lee, C. M. Liddell and I. Cohen, *Physical Review Letters*, 2008, **101**, 058302.

42 A. van Blaaderen, R. Ruel and P. Wiltzius, *Nature*, 1997, **385**, 321–324.

43 T. Dasgupta, J. R. Edison and M. Dijkstra, *The Journal of Chemical Physics*, 2017, **146**, 074903.

44 V. W. A. d. Villeneuve, L. Derendorp, D. Verboekend, E. C. M. Vermolen, W. K. Kegel, H. N. W. Lekkerkerker and R. P. A. Dullens, *Soft Matter*, 2009, **5**, 2448–2452.

45 W. T. M. Irvine, A. D. Hollingsworth, D. G. Grier and P. M. Chaikin, *Proceedings of the National Academy of Sciences*, 2013, **110**, 15544–15548.

46 C. E. Cash, J. Wang, M. M. Martirossyan, B. K. Ludlow, A. E. Baptista, N. M. Brown, E. J. Weissler, J. Abacousnac and S. J. Gerbode, *Physical Review Letters*, 2018, **120**, 018002.

47 F. A. Lavergne, A. Curran, D. G. A. L. Aarts and R. P. A. Dullens, *Proceedings of the National Academy of Sciences*, 2018, **115**, 6922–6927.

48 B. v. d. Meer, L. Filion and M. Dijkstra, *Soft Matter*, 2016, **12**, 3406–3411.

49 B. v. d. Meer, M. Dijkstra and L. Filion, *Soft Matter*, 2016, **12**, 5630–5635.

50 A. R. Tao, S. Habas and P. Yang, *Small*, 2008, **4**, 310–325.

51 S. Cheong, J. D. Watt and R. D. Tilley, *Nanoscale*, 2010, **2**, 2045–2053.

52 M. Grzelczak, J. Pérez-Juste, P. Mulvaney and L. M. Liz-Marzán, *Chemical Society Reviews*, 2008, **37**, 1783–1791.

53 T. Mura, in *Micromechanics of defects in solids*, Springer Netherlands, 1987, pp. 1–73.

54 Y. P. Chiu, *Journal of Applied Mechanics*, 1977, **44**, 587–590.

55 D. C. Wallace, *Thermodynamics of Crystals*, Wiley, New York, 1972.

56 J. A. Anderson, C. D. Lorenz and A. Travesset, *Journal of Computational Physics*, 2008, **227**, 5342–5359.

57 J. Glaser, T. D. Nguyen, J. A. Anderson, P. Lui, F. Spiga, J. A. Millan, D. C. Morse and S. C. Glotzer, *Computer Physics Communications*, 2015, **192**, 97–107.

58 J. Weeks, D. Chandler and H. C. Andersen, *The Journal of Chemical Physics*, 1971, **54**, 5237–5247.

59 G. J. Martyna, M. E. Tuckerman, D. J. Tobias and M. L. Klein, *Molecular Physics*, 1996, **87**, 1117–1157.

60 B. VanSaders, J. Dshemuchadse and S. C. Glotzer, *Physical Review Materials*, 2018, **2**, 063604.

61 A. A. Gusev, M. M. Zehnder and U. W. Suter, *Phys. Rev. B*, 1996, **54**, 1–4.

62 T. D. Nguyen, C. L. Phillips, J. A. Anderson and S. C. Glotzer, *Computer Physics Communications*, 2011, **182**, 2307–2313.

63 H. Risken and H. D. Vollmer, *Zeitschrift für Physik B Condensed Matter*, 1979, **33**, 297–305.

64 A. Stukowski, *Modelling and Simulation in Materials Science and Engineering*, 2010, **18**, 015012.

65 A. Stukowski and K. Albe, *Modelling and Simulation in Materials Science and Engineering*, 2010, **18**, 085001.

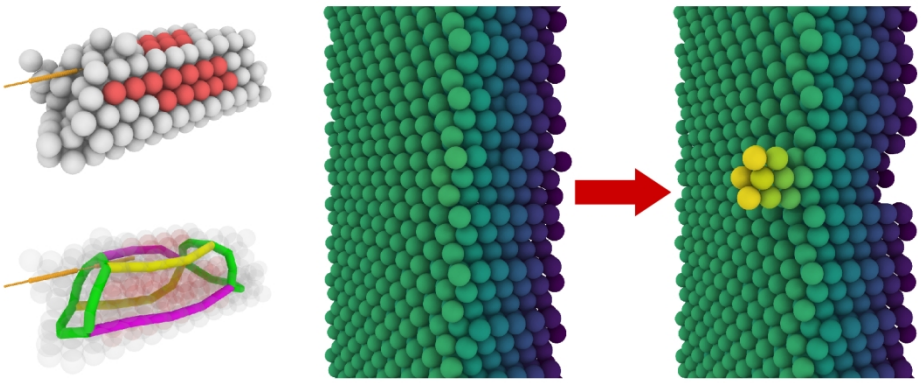

Table of Contents Entry: We report a novel method for designing active interstitials capable of driving colloidal dislocations to glide.